The Formation and Evolution of Prestellar Cores

Formation of Prestellar Cores: Observations and Theory

Edited by
PHILIPPE ANDRE[1], SHANTANU BASU[2], and SHU-ICHIRO INUTSUKA[3]
(1) Service d'Astrophysique, UMR AIM, CEA/DSM - CNRS - Univ. Paris 7, CEA Saclay, France
(2) Department of Physics and Astronomy, Univ. of Western Ontario, London, Canada
(3) Department of Physics, Graduate School of Science, Kyoto Univ., Japan

Contents

11

The Formation and Evolution of Prestellar Cores

11.1 Introduction: Dense cores and the origin of the IMF

Stars form from the gravitational collapse of dense cloud cores in the molecular interstellar medium of galaxies. Studying and characterizing the properties of dense cores is thus of great interest to gain insight into the initial conditions and initial stages of the star formation process.

Our observational understanding of low-mass dense cores has made significant progress in recent years and three broad categories of cores can now be distinguished within nearby molecular clouds, which possibly represent an evolutionary sequence: starless cores, prestellar cores, and "Class 0" protostellar cores. Starless cores are possibly transient concentrations of molecular gas and dust without embedded young stellar objects (YSOs), typically observed in tracers such as $C^{18}O$ (e.g. Onishi et al. 1998), NH_3 (e.g. Jijina, Myers, & Adams 1999), or dust extinction (e.g. Alves et al. 2007), and which do not show evidence of infall. Prestellar cores are also starless ($M_\star = 0$) but represent a somewhat denser and more centrally-concentrated population of cores which are self-gravitating, hence unlikely to be transient. They are typically detected in (sub)millimeter dust continuum emission and dense molecular gas tracers such as NH_3 or N_2H^+ (e.g. Ward-Thompson et al. 1994; Benson & Myers 1989; Caselli et al. 2002), often seen in absorption at mid- to far-infrared wavelengths (e.g. Bacmann et al. 2000, Alves et al. 2001), and frequently exhibit evidence of infall motions (e.g. Gregersen & Evans 2000). Conceptually, all prestellar cores are starless but only a subset of the starless cores evolve into prestellar cores; the rest are presumably "failed" cores that eventually disperse and never form stars. In practice, prestellar cores are characterized by large density contrasts over the local background medium. Specifically, the mean densities of observed prestellar cores exceed the mean densities of their parent clouds by a factor $\gtrsim$ 5–10,

while their mean column densities exceed the background column densities by a factor $\gtrsim$ 2. For comparison, a critical self-gravitating Bonnor-Ebert isothermal spheroid has a mean density contrast $\bar{\rho}_{\rm BE}/\rho_{\rm ext} \sim 2.4$ (e.g. Lombardi & Bertin 2001) and a mean column density contrast $\bar{\Sigma}_{\rm BE}/\Sigma_{\rm ext} \sim 1.5$ over the external medium.

Finally, Class 0 cores/objects are young accreting protostars observed early after point mass formation while most of the mass of the system is still in the form of a dense core/envelope as opposed to a YSO ($M_\star \ll M_{\rm env}$) (André, Ward-Thompson, Barsony 1993). They are believed to result from the gravitational collapse of prestellar cores. Class 0 protostars themselves evolve into Class I objects with $M_{\rm env} < M_\star$ (Lada 1987; André & Montmerle 1994) as the protostellar envelope dissipates through accretion and ejection of circumstellar material. Class I objects subsequently evolve into (Class II and Class III) pre-main sequence stars surrounded by a circumstellar disk (optically thick and optically thin in the near-/mid-IR, respectively), but lacking a dense circumstellar envelope ($M_{\rm env} \sim 0$).

Improving our understanding of the formation and evolution of dense cores in molecular clouds is crucially important since there is now good evidence that these early stages largely control the origin of the stellar initial mass function (IMF). Indeed, observations indicate that the prestellar core mass function resembles the IMF (see § 11.2 below), suggesting that the effective reservoirs of mass required for the formation of individual stars are already selected at the prestellar core stage. Furthermore, it is at the very end of the prestellar stage that multiple systems are believed to form and during the protostellar stage that a fraction of the prestellar core mass reservoir is accreted by the central protostellar components as a result of the accretion/ejection process.

11.2 Link between the prestellar core mass function and the IMF

Wide-field (sub)mm dust continuum mapping is a powerful tool to take a census of prestellar dense cores and young protostars within star-forming clouds. The advent of large-format bolometer arrays on (sub)millimeter radiotelescopes such as the IRAM 30m and the JCMT has led to the identification of numerous cold, compact condensations that do not obey the Larson (1981) self-similar scaling laws of molecular clouds and are intermediate in their properties between diffuse CO clumps and infrared young stellar objects (cf. André et al. 2000 and Ward-Thompson et al. 2007 for reviews). As an example, Fig. 11.1 shows the condensations found by Motte et al. (2001) at 850 μm in the NGC 2068 protocluster (Orion B). Such highly

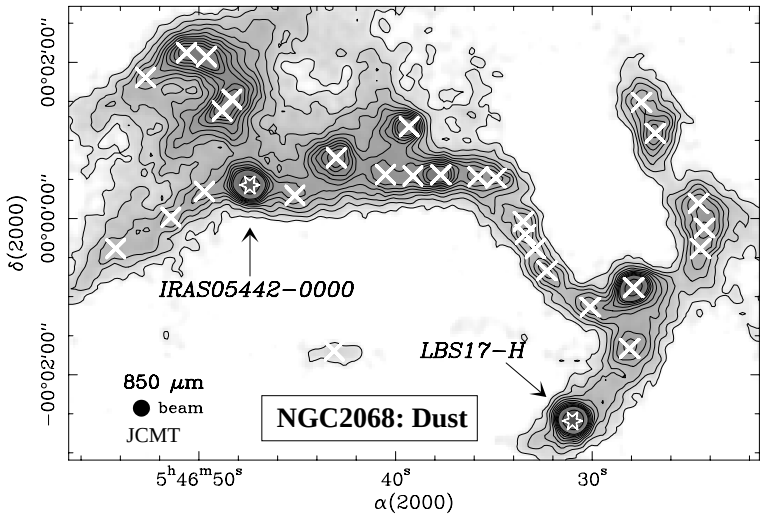

Fig. 11.1. SCUBA 850 μm dust continuum map of the NGC 2068 protocluster extracted from the mosaic of Orion B by Motte et al. (2001). A total of 30 compact prestellar condensations (marked by crosses), with masses between $\sim 0.4\,M_\odot$ and $\sim 4.5\,M_\odot$, are detected in this ~ 1 pc $\times$ 0.7 pc field.

concentrated (sub)millimeter continuum condensations are at least 3 to 6 orders of magnitude denser than typical CO clumps (e.g. Kramer et al. 1998) and feature large ($\gg 50\%$) mean column density contrasts over their parent background clouds, strongly suggesting they are self-gravitating. The latter is directly confirmed by line observations in a number of cases. When available, the virial masses of the condensations indeed agree within a factor of ~ 2 with the masses derived from the (sub)millimeter dust continuum (e.g. André et al. 2007). A small fraction of these condensations lie at the base of powerful jet-like outflows and correspond to Class 0 objects. However, the majority of them are starless/jetless and appear to be the immediate prestellar progenitors of individual protostars or protostellar systems.

In particular, as first pointed out by Motte, André, Neri (1998) in the case of the ρ Ophiuchi (L1688) cloud, the mass distribution of these starless dust continuum condensations is remarkably similar in shape to the stellar IMF (see Fig. 11.2). This was consistently found by a number of independent groups in the past few years (e.g. Testi & Sargent 1998; Johnstone et al. 2000, 2001; Motte et al. 2001; Stanke et al. 2006; Enoch et al. 2006; Nutter & Ward-Thompson 2007) in nearby star-forming regions such as ρ Ophi-

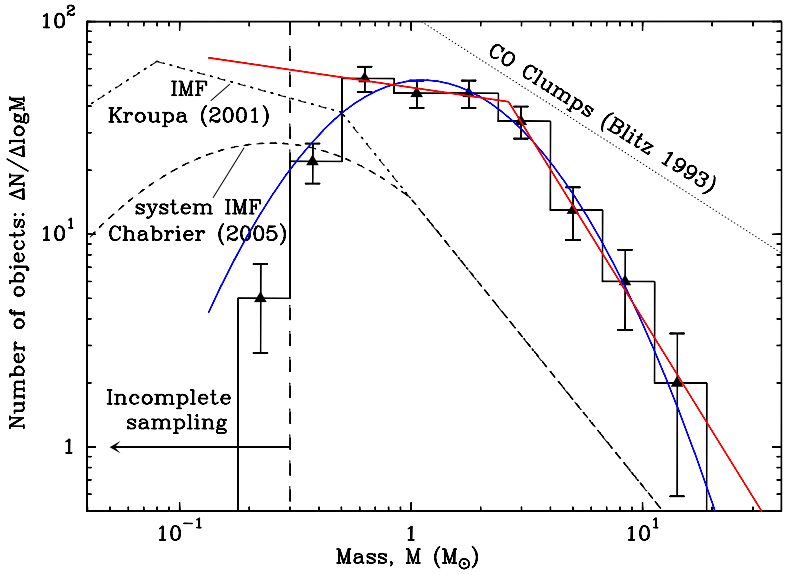

Fig. 11.2. Differential (dN/dlogM) mass distribution of the 229 starless dust continuum condensations detected at 850 μm with SCUBA in the Orion A/B cloud complex excluding the crowded OMC1 and NGC 2024 regions (histogram with error bars – from Motte et al. 2001, Johnstone et al. 2001, and Nutter & Ward-Thompson 2007). This prestellar core sample is estimated to be complete down to $\sim 0.3\,M_{\odot}$. A two-segment power law fit and a lognormal fit are shown for comparison. For reference, the dash-dotted curve shows the shape of the single-star IMF (e.g. Kroupa 2001) and the dashed curve corresponds to the IMF of multiple systems (e.g. Chabrier 2005). The dotted line shows a dN/dlogM $\propto M^{-0.6}$ power-law distribution corresponding to the typical mass spectrum found for low-density CO clumps (see Blitz 1993 and Kramer et al. 1998).

uchi, Serpens, Orion A & B, and Perseus. In all of these clouds, the observed prestellar core mass function (CMF) is consistent with the Salpeter (1955) power-law IMF at the high-mass end (dN/dlogM $\propto M^{-1.35}$), and thus significantly steeper than the mass distribution of diffuse CO clumps (dN/dlogM $\propto M^{-0.6}$ over at least three decades in mass – e.g. Blitz 1993; Kramer et al. 1998). The difference presumably arises because CO clumps are primarily structured by supersonic turbulence (e.g. Elmegreen & Falgarone 1996) while prestellar condensations are largely free of supersonic turbulence and clearly shaped by self-gravity (e.g. Motte et al. 2001, André et al. 2007 and § 11.3.2 below). The slope of the observed CMF becomes shallower than the Salpeter power law and more similar to the slope of the typical CO clump mass distribution at the low-mass end. Based on the

results of present core surveys, the entire prestellar CMF can generally be fit equally well with either a two-segment broken power law or a lognormal distribution down to the completeness limit of the observations. This is illustrated in Fig. 11.2 which shows the differential CMF in log-log format for a sample of 229 starless submillimeter continuum cores in the Orion A/B complex identified in the SCUBA surveys of Motte et al. (2001) and Johnstone et al. (2001, 2006).

Note that there is some discussion in the literature (e.g. Reid & Wilson 2006) as to whether the differential or the cumulative form of the CMF should be used. The differential form is more intuitive to interpret as it can be fit using the standard least-squares technique after assigning simple Poisson error bars. It is however inadequate when the total number of objects is small ($\lesssim 100$) as it is significantly affected by the arbitrary choice of mass bins. The cumulative form, which is independent of binning, is preferable when dealing with small samples, but some care must be taken when comparing it with model distributions based on least-squares fits (cf. Reid & Wilson 2006). In practice, using the non-parametric Kolmogorov-Smirnov (K-S) test to compare the cumulative form of the CMF with model distributions is more reliable than least-squares fitting. The K-S test confirms that, within statistical uncertainties, the prestellar CMF observed in the above-mentioned nearby clouds is indistinguishable in shape from the stellar IMF, although the significance remains limited by the relatively small size of present prestellar core samples. The K-S test also shows that the observed CMF differs from the shallow power-law mass distribution of CO clumps at a very high significance level (for instance, in the Orion case illustrated in Fig. 11.2, the probability that the two mass distributions are statistically similar in shape is only $P \approx 2 \times 10^{-6}$).

In addition, the median prestellar core mass observed in regions such as ρ Ophiuchi and Orion ($\sim 0.2 - 1.5\,M_\odot$) is only slightly larger than the characteristic $\sim 0.5\,M_\odot$ set by the peak of the IMF in dN/dlogM format. Such a close resemblance of the CMF to the IMF in both shape and mass scale is consistent with the view that the prestellar condensations identified in (sub)millimeter dust continuum surveys are about to form stars on a one-to-one basis, with a fixed and relatively high local efficiency, i.e., $\epsilon_{\rm core} \equiv M_\star/M_{\rm core} \gtrsim 30 - 50\%$.

Interestingly, in a recent near-IR extinction imaging study of the Pipe dark cloud, Alves et al. (2007) found a population of 159 starless cores whose mass distribution similarly follows the shape of the IMF. This finding is reminiscent of the CMF results obtained from the (sub)millimeter dust continuum, although it is important to stress that most of the starless cores

in the Pipe Nebula are gravitationally unbound objects confined by external pressure (Lada et al. 2008). Hence, they do not qualify as prestellar cores and a large fraction of them may never evolve into stars. Assuming nevertheless that most of them will evolve into self-gravitating prestellar cores and subsequently collapse into stars, the Alves et al. (2007) result suggests that the IMF may be determined even earlier than the prestellar stage.

Appealing as a direct connection between the prestellar CMF and the IMF might be, several caveats should be kept in mind. First, although core mass estimates based on optically thin (sub)millimeter dust continuum emission are straightforward, they rely on uncertain assumptions about the *dust (temperature and emissivity) properties* (e.g. Stamatellos et al. 2007a). Second, current determinations of the CMF are limited by small-number statistics in any given cloud and may be affected by incompleteness at the low-mass end (e.g. Johnstone et al. 2000). With *Herschel*, the future submillimeter space telescope to be launched in 2008, it will be possible to dramatically improve on the statistics and to largely eliminate the mass uncertainties through direct measurements of the dust temperatures (cf. André & Saraceno 2005). Third, in some regions such as the ρ Ophiuchi cloud, the shape of the CMF is in better agreement with the IMF of individual field stars than with the IMF of multiple systems (e.g. André et al. 2007). This is surprising since the spatial resolution of current surveys for prestellar cores ($\sim$ 2000 AU at best) is not sufficient to probe core multiplicity. Furthermore, multiple systems are believed to form *after* the prestellar stage by subsequent dynamical fragmentation during the collapse phase, close to the time of protostar formation (e.g. Goodwin et al. 2007). Thus, one would expect the masses of prestellar cores to be more directly related to the masses of multiple systems than to the masses of individual stars. It is possible that a fraction at least of the cores observed at masses lower than the peak of the CMF in dN/dlogM format (e.g., $\sim 1.1\,M_{\odot}$ in Fig. 11.2) are not gravitationally bound, hence not prestellar in nature (cf. André et al. 2007).

Last but not least, there is a potential timescale problem. As pointed out by Clark, Klessen, & Bonnell (2007), if the lifetime of prestellar cores depends on their mass, then the observed mass distribution is not necessarily representative of the intrinsic CMF (see also Elmegreen 2000). This is due to the fact that an observer is more likely to detect long-lived cores than short-lived cores. In practice, however, the mean densities of prestellar cores are essentially uncorrelated with their masses, so that there is no systematic dependence of the dynamical timescale on the mass. The importance of the potential timescale bias can be assessed by considering a *weighted* core

mass function in which each core is assigned a weight equal to $\frac{\langle t_{\rm ff} \rangle}{t_{\rm ff}} = \frac{\bar{\rho}^{1/2}}{\langle \bar{\rho}^{1/2} \rangle}$ (instead of 1), where $\langle t_{\rm ff} \rangle$ is the average free-fall time of the sampled cores. Such a weighting makes it possible to recover the intrinsic shape of the CMF if the lifetime of each core is proportional to its free-fall time. André et al. (2007) applied this technique to the sample of 57 starless dust continuum condensations identified by Motte et al. (1998) at 1.2 mm in the ρ Ophiuchi cloud. In this case, the above-mentioned weighting does not change the high-mass end of the CMF and only affects the low-mass end: it renders the entire ρ Oph CMF derived above the $\sim 0.1\,M_\odot$ completeness level remarkably consistent with a single, Salpeter power-law mass distribution (see Fig. 8 of André et al. 2007). We conclude that the steep, Salpeter-like slope of the CMF at the high-mass end is robust, but that the departure from a single power-law distribution at the low-mass end, in the form of a break near the median core mass (cf. Fig. 11.2), is less robust.

Despite these limitations, the observational findings summarized in this section are very encouraging as they support scenarios according to which the bulk of *the IMF is partly determined by pre-collapse cloud fragmentation* (e.g. Larson 1985, 2005; Elmegreen 1997; Padoan & Nordlund 2002). The finding that the high-mass end of the prestellar CMF is substantially steeper than the dN/dlogM $\propto$ M$^{-0.6}$ mass distribution of low-density CO clumps is very significant: while most of the mass of the low-density CO medium is contained in the largest, most massive clumps, most of the prestellar mass destined to evolve into stars is in small, low-mass cores. Clearly, one of the keys to the problem of the origin of the IMF lies in a good understanding of the processes responsible for the formation of prestellar cores/condensations out of low-density structures within molecular clouds. However, it is likely that additional processes, such as subfragmentation into binary/multiple systems and more generally mechanisms controlling the value of the star formation efficiency at the core level ($\epsilon_{\rm core}$), also play an important role and, in particular, are required to generate the low-mass ($M < 0.3\,M_\odot$) end of the IMF (cf. Bate et al. 2003, Ballesteros-Paredes et al. 2006). In the following sections, we discuss core formation and core subfragmentation models in turn.

11.3 Core formation models vs. observational constraints

The mechanisms by which prestellar cores form and evolve in molecular clouds are the subject of a major theoretical debate at the moment. There is little doubt that self-gravity ultimately plays a dominant role and it has even been proposed that dense cores may form by purely gravitational frag-

mentation (e.g. Larson 1985; Hartmann 2002). However, the respective roles of magnetic fields and interstellar turbulence in regulating the core/star formation process are highly controversial. In particular, the classical picture of slow, quasi-static core formation by ambipolar diffusion in magnetically-supported clouds (e.g. Mouschovias 1987; Shu et al. 1987, 2004) has been seriously challenged by a new, much more dynamic paradigm, which emphasizes the role of supersonic turbulence in supporting clouds on large scales and generating density fluctuations on small scales (e.g. Padoan & Nordlund 2002; Mac Low & Klessen 2004). Conceptually, core formation models may be conveniently divided up into four categories, depending on whether linear or non-linear (turbulent) perturbations initiate core formation, and on whether magnetic fields are dynamically dominant or not (see Table 11.1 below). In this classification, the "standard" picture and the new turbulent paradigm correspond to two extreme models, according to which cores form by magnetically-regulated gravitational fragmentation and super-Alfvénic turbulent fragmentation, respectively. In all turbulent models, cores are initially formed by cloud material compressed by shocks arising from supersonic turbulence. There are however several versions of the dynamic picture of core/star formation which mainly differ in the way they explain the origin of the IMF. In the Padoan & Nordlund (2002) scenario, the IMF is almost entirely set by the properties of interstellar turbulence at the prestellar stage, while in the alternative model proposed by Bate & Bonnell (2005), turbulence is largely irrelevant for the IMF which originates from competitive accretion and dynamical interactions at the protostellar stage. The Klessen & Burkert (2000) scenario is intermediate between these two extremes in that both turbulence and dynamical interactions play a role in shaping the IMF. The various turbulent models also differ depending on whether the turbulence is freely decaying (e.g. Tilley & Pudritz 2007) or continuously driven (e.g. Vázquez-Semadeni et al. 2005).

11.3.1 Theoretical description of cloud fragmentation models

The classical problems of fragmentation of a sheet-like layer or a cylinder are relevant to star formation because they show that there is a *preferred* scale of gravitational fragmentation as soon as one considers a structured (i.e., flattened or filamentary) region with some scale length H (see Larson 1985). This is not the case for a uniform medium, in which case the Jeans analysis shows that the largest possible scale has the fastest growth rate. Sheets and filaments can be easily generated by the formation process of the molecular cloud itself or by subsequent internal turbulent or gravitational

motions. For isothermal sheets, $H = c_{\rm s}^2/(\pi G\Sigma)$, where $c_{\rm s}$ is the isothermal sound speed, and Σ is the column density of the sheet. For highly flattened sheets, the preferred fragmentation scale is $\lambda_m = 2\pi H$, while for a layer with the extended isothermal atmosphere calculated by Spitzer (1942), $\lambda_m = 4.4\pi H$ (Simon 1965). These two length scales likely bracket the possibilities for more realistic isothermal non-magnetic sheet-like configurations. The growth time of the fragmentation instability is essentially the dynamical timescale $t_{\rm d} \simeq H/c_{\rm s}$ for the cases described above, and is more generally identified with the free-fall timescale $t_{\rm ff} \simeq 1/\sqrt{G\rho}$ that applies to both unpressured sheets and those confined by a strong external pressure.

However, purely gravitational fragmentation instability of an entire molecular cloud on the dynamical timescale given by the mean column density and temperature is ruled out (Zuckerman and Palmer 1974), due to the observed low efficiency of Galactic star formation. Nevertheless, it remains a relevant concept to understanding fragmentation in the cluster-forming subregions of molecular clouds. A proposed explanation for the low efficiency of star formation is the so-called "standard model" of star formation (Shu, Adams, & Lizano 1987; Mouschovias 1987), in which cores are formed on a diffusive timescale (much longer than than a dynamical timescale), due to the ambipolar drift of neutrals past dynamically dominant magnetic fields. This mode of star formation is often erroneously labeled as "isolated" star formation. In reality, ambipolar diffusion driven core formation is also a fragmentation process as surely as its nonmagnetic counterpart - the difference is primarily in the timescale of evolution. One may however make the following distinction based on the mass-to-magnetic flux ratio, M/Φ, compared to the critical value, $(M/\Phi)_{\rm crit}$, necessary for support against gravitational collapse. Molecular cloud envelopes may be magnetically dominated, with subcritical to transcritical mass-to-flux ratios, i.e., $\mu_{\rm env} \equiv (M/\Phi)\,/\,(M/\Phi)_{\rm crit} \leq 1$. Cloud envelopes also have low mean density and relatively high levels of ionization, and thereby evolve on such a long timescale for fragmentation that no runaway has essentially occurred by the time we observe the clouds. Conversely, the cluster-forming cores (and also regions of weak clustering found in the Taurus molecular cloud) may be magnetically supercritical with $\mu_{\rm clus} > 1$ and also have greater mean density, resulting in fragment formation on relatively shorter timescales and lengthscales.

For the above reasons and because Zeeman measurements (see the compilation of Crutcher 1999 and § 11.3.2.3 below) establish that mass-to-flux ratios are clustered about the critical value, it is important to study cloud fragmentation including the effect of dynamically significant magnetic fields

and also ambipolar diffusion, if possible. Magnetized sheets can be studied most easily in two limits. If the formation process of the sheet is by dynamical compression, say from stellar winds or supernovae, the ambient interstellar magnetic field may be swept up into the expanding shell and be oriented primarily in the plane of the sheet. Conversely, if self-gravity plays an important role in the formation of the sheet, then it will be flattened along the mean direction of the magnetic field.

When the magnetic field is in the plane of the sheet, the character of fragmentation and the fate of the cloud can be further categorized into two subcases (Nagai, Inutsuka, & Miyama 1998). If the geometrical thickness of the sheet is comparable to (or larger than) the natural scale height ($\sim c_{\rm s}/\sqrt{G\rho_{\rm c}}$), or equivalently, if the ambient pressure is much smaller than the midplane pressure, compressional motions along the magnetic field lines result in the formation of filamentary clouds elongated perpendicular to the field lines. The line-mass (mass per unit length) of the filament is larger than that of the (isothermal) equilibrium filament so that collapse toward the axis of the filament continues until temperature increases (Inutsuka & Miyama 1992). In this case, the characteristic (i.e., minimum) mass scale for fragmentation is determined by the final fragmentation of the filamentary cloud, and significantly smaller than the initial Jeans mass of the sheet (Inutsuka & Miyama 1997). The resulting mass scale can be called "the minimum Jeans mass" and its dependence on the initial temperature and metallicity of the cloud was discussed by Masunaga & Inutsuka (1999). The expected core mass function was analytically derived by Inutsuka (2001) using the Press-Schechter formalism. The overall timescale of the whole process is on the order of the initial free-fall time ($t_{\rm ff} \sim 1/\sqrt{G\rho_{\rm c}}$).
In contrast, if the sheet-like cloud is confined by strong external pressure due to an ambient warm (or hot) medium, the thickness of the sheet is smaller than $\sim c_{\rm s}/\sqrt{G\rho_{\rm c}}$. The timescale for fragmentation is still on the order of the gravitational free-fall time $t_{\rm ff}$, but sound waves can now propagate many times across the (thin) sheet within this timescale. Thus, the fragmentation is in an incompressible mode and the axes of the resulting filaments are parallel to the direction of the magnetic field. In this case, the filaments may fragment into cores whose masses can be smaller than the Jeans mass. In effect, this second case provides a mechanism for generating gravitationally stable cores (Inutsuka & Miyama 1997).

When the magnetic field is oriented perpendicular to the sheet, recent simulations of cloud fragmentation which include ambipolar diffusion have allowed an extensive parameter study of the interplay of magnetic fields, ambipolar diffusion, and turbulence in the formation of cores (Basu & Ciolek

Table 11.1. *Summary of main features of core formation models.*

Core Formation Scenarios		
Models	Gravitational Fragmentation (linear perturbations)	Turbulent Fragmentation (non-linear perturbations)
Weak B	Short (few Myr) timescale infall mildly supersonic ordered curved field lines initial CMF very narrow	Very short (< Myr) timescale infall highly supersonic field lines distorted initial CMF is broad, IMF-like
Strong B	Long ($\sim$ 10 Myr) timescale subsonic infall small field line curvature initial CMF very narrow	Short (few Myr) timescale subsonic relative infall and supersonic systematic speeds ordered field lines initial CMF is broad, IMF-like

2004; Basu, Ciolek, & Wurster 2008). Given the standard cosmic-ray induced ionization fraction $x_i \simeq 10^{-7}(n/10^4\,\mathrm{cm}^{-3})^{-1/2}$ (Elmegreen 1979; Nakano 1979), there is an observationally distinguishable difference between subcritical and supercritical fragmentation. Subcritical fragmentation leads to subsonic infall motions onto cores and within them, while supercritical cloud fragmentation leads to extended supersonic infall on the core scale ~ 0.1 pc and even beyond.

Figure 11.3 shows a comparison of column density structure and velocity vectors for four different models (from Basu, Ciolek, & Wurster 2008; Basu et al. 2008). Each image is shown at the time of runaway collapse of the first supercritical dense core that forms in the simulation, with a column density enhancement of a factor of 10. The top two images are for subcritical (left) and supercritical (right) clouds evolving from linear initial perturbations. The bottom two images are for subcritical (left) and supercritical (right) clouds evolving from highly nonlinear (turbulent) initial conditions. Each image represents a physically distinct path to core/star formation. Velocity vectors are overlaid, although the normalizations may differ (see caption). The subcritical models have $\mu_0 = 0.5$ (i.e., the mass-to-flux ratio is half the critical value) and the supercritical models have $\mu_0 = 2$. Amongst the gravitational fragmentation models (linear initial perturbations), there is extended and mildly supersonic motions only in the supercritical model, whereas the subcritical model has a maximum speed of only $\sim 0.4c_\mathrm{s}$. For the subcritical gravitational fragmentation model the runaway collapse to the first core occurs at a time 7.4 Myr, whereas for the supercritical model it occurs at 0.83 Myr, assuming a background column density 10^{22} cm^{-2}

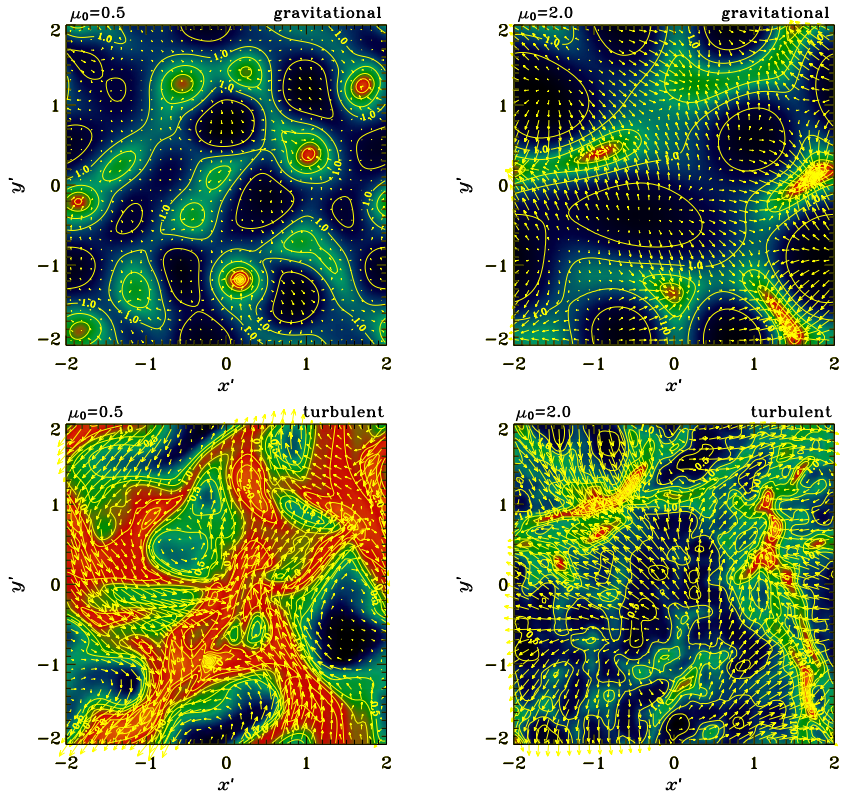

Fig. 11.3. Image and contours of column density and velocity vectors of neutrals, for four different models at the time of runaway collapse of the first supercritical dense core (Basu, Ciolek, & Wurster 2008; Basu et al. 2008). Top left: gravitational fragmentation for a subcritical model $\mu_0 = 0.5$. Top right: the same for a supercritical model with $\mu_0 = 2.0$. Bottom left: turbulent fragmentation for $\mu_0 = 0.5$. Bottom right: turbulent fragmentation for $\mu_0 = 2.0$. The color table is applied to the logarithm of column density and the contour lines represent values of column density enhancement in multiplicative increments of $2^{1/2}$, having the values [0.7,1.0,1.4,2,2.8,4.0,...]. The horizontal or vertical distance between tips of velocity vectors corresponds to a speed $0.5\,c_{\rm s}$ in the top panels, to $1.0\,c_{\rm s}$ in the bottom left panel, and to $3.0\,c_{\rm s}$ in the bottom right panel. Spatial coordinates are normalized to $2\pi H$, the wavelength of maximum growth rate in the limit of no magnetic field and external pressure.

and temperature 10 K. Fragmentation of a transcritical ($\mu_0 \simeq 1$) cloud is qualitatively unique in that the fragmentation spacing is much larger than the typical value $\simeq 2\pi H$ that is valid for both highly supercritical and highly subcritical clouds (Ciolek & Basu 2006). The timescale of transcritical fragmentation is intermediate to the subcritical and supercritical cases, but closer to the former. Here, we focus primarily on the distinction be-

tween decidedly subcritical and supercritical clouds. The bottom panels of Fig. 11.3 show the corresponding $\mu_0 = 0.5$ (left) and $\mu_0 = 2$ (right) models, now with turbulent initial perturbations with rms amplitude $v_a = 2c_{\rm s}$ in each of v_x and v_y. The power spectrum is such that $v_k^2 \propto k^{-4}$, so most of the energy is in the largest scale modes: the result is immediate large-scale compressive motions in the cloud. The $\mu_0 = 0.5$ model undergoes rapid ambipolar diffusion during the first compression, but still rebounds due to stored magnetic energy. It subsequently oscillates several times before continuing ambipolar diffusion causes runaway collapse in the highest density region. The total time for this process is 1.2 Myr, similar to that of supercritical gravitational fragmentation. In contrast, the $\mu_0 = 2$ model goes into prompt collapse during the first compression, on a timescale of merely 4.0×10^4 yr $= 0.04$ Myr. Systematic supersonic motions exist in both turbulent models, but the relative infall is generally subsonic in the subcritical model. A comparison of the two bottom panel images shows that the supercritical model is extremely filamentary, while the subcritical model is much less so since it has had a chance to rebound from the initial compression. These turbulent simulations are done in the thin-disk approximation and are consistent with the earlier results of Li & Nakamura (2004) and Nakamura & Li (2005), also done using the same approximation. Recent fully three-dimensional simulations (Kudoh et al. 2007; Kudoh & Basu 2008) also confirm the results. A summary of main outcomes of the four different modes of core/star formation is given in Table 11.1.

The results described above are used to generate statistics of core masses, sizes, shapes, etc. Each model with a unique set of parameters is run ~ 100 times in order to generate a meaningful measure of the various outcomes arising from different realizations of the initial random perturbations. Thresholding techniques are used to identify cores - for details of the technique, see Basu, Ciolek, & Wurster (2008). Figure 11.4 shows a comparison of the initial core mass function (CMF) for supercritical models with $\mu_0 = 2$ but without and with turbulent initial perturbations, respectively. We emphasize these are *initial* CMF's because they reflect the status of cores at the time that the first supercritical dense core undergoes runaway collapse. The clear distinction to be made between the two models is that the linear initial perturbation case (left panel) has an extremely sharp peak (consistent with a preferred mass scale for fragmentation in the linear theory), although there is a broader tail at the low mass end due to some cores that are very young and just emerging above the threshold. In contrast, the turbulent initial condition case develops a broad tail of high mass cores, due to much of the turbulent power being on large scales. However, the high mass cores

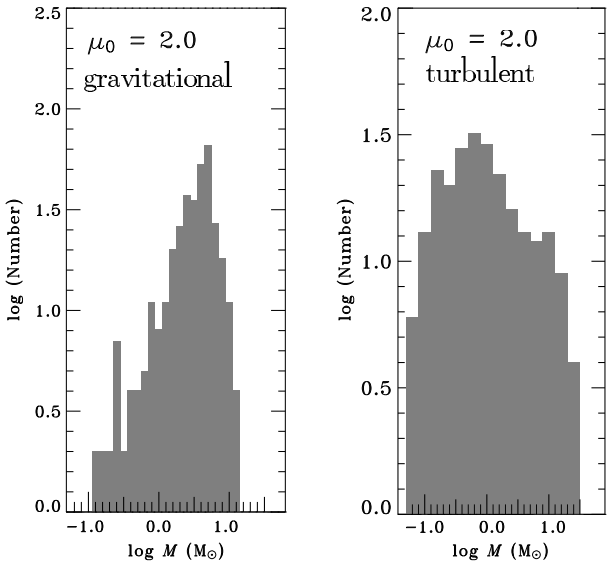

Fig. 11.4. Histograms of masses contained within regions with column density enhancement above a factor of two, measured at the end point of simulations with $\mu_0 = 2.0$. The left panel corresponds to gravitational fragmentation and the right panel corresponds to turbulent fragmentation. See text for details. Each figure is obtained from the compilation of results of a large number of simulations. The bin width is 0.1.

often have quite disturbed structures (see Fig. 11.3 lower panels) and it is not clear that they would subsequently collapse monolithically.

The narrow initial CMF seems to be a problem for purely gravitational fragmentation models. However, a broader distribution may yet be possible if the newly formed cores continue to accrete from their environment. If the accretion from the environment is nonuniform from core to core, an initially narrow and/or lognormal CMF may become skewed so that a high mass tail develops. For example, Basu & Jones (2004) have generalized an earlier result of Myers (2000) and shown that an initially lognormal CMF and an exponential distribution of subsequent accretion times from the cloud results in a CMF that is like a lognormal at low masses but has a power-law tail at high masses. The model formally requires that the accretion rate onto a core is linearly proportional to the instantaneous core mass. Additionally, Basu & Jones (2004) show that a different accretion law can also lead to a broadened near-power-law tail.

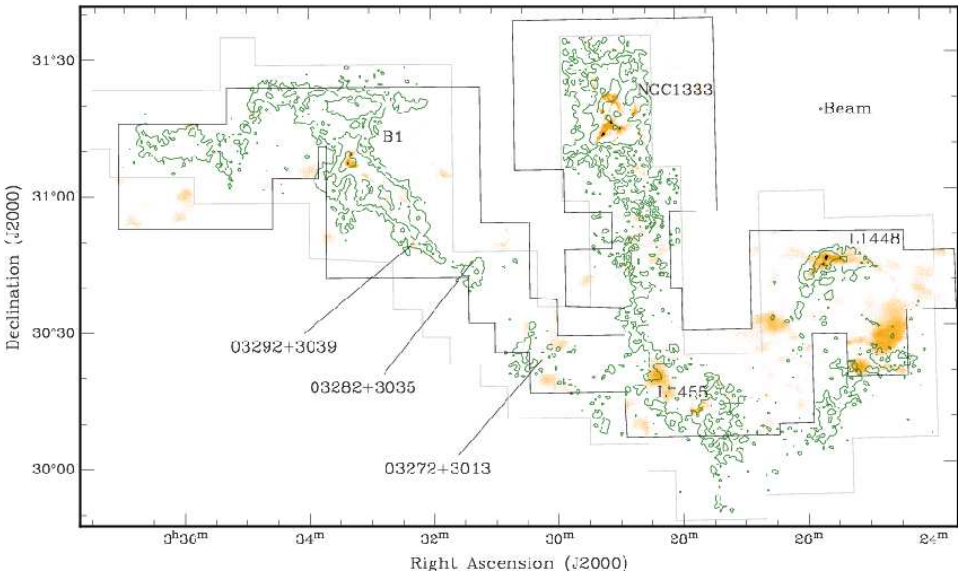

Fig. 11.5. SCUBA 850 μm dust continuum map (colorscale) of the Western part of the Perseus cloud complex. Contours of $C^{18}O$(1-0) integrated intensity are overlaid. The black boundary indicates the total area mapped with SCUBA. Note that dust continuum cores are detected only localized sub-regions, such as NGC 1333, within the complex. (From Hatchell et al. 2005)

11.3.2 Observational diagnostics

In principle, it should be possible to discriminate between these various core formation scenarios based on detailed observational studies of the characteristics of prestellar cores and young protostars.

11.3.2.1 Core formation efficiency and spatial distribution from surveys

A number of very large submillimeter continuum surveys of nearby cloud complexes have been completed recently which provide the spatial distribution of cores within these complexes and set constraints on the efficiency of the core formation process (e.g. Johnstone et al. 2004, Hatchell et al. 2005, Enoch et al. 2006, Motte et al. 2007). As an illustration, Figure 11.5 shows part of the 3 deg^2 SCUBA 850 μm survey of the Perseus cloud complex by Hatchell et al. (2005). Such extensive surveys show that prestellar cores and Class 0 protostars are found in localized sub-regions within molecular clouds which occupy only a very small fraction of their volume. These localized active sub-regions often correspond to cluster-forming clumps associated with embedded near-IR clusters. On this basis, it has been suggested that there may be a threshold in background column density (or equivalently visual

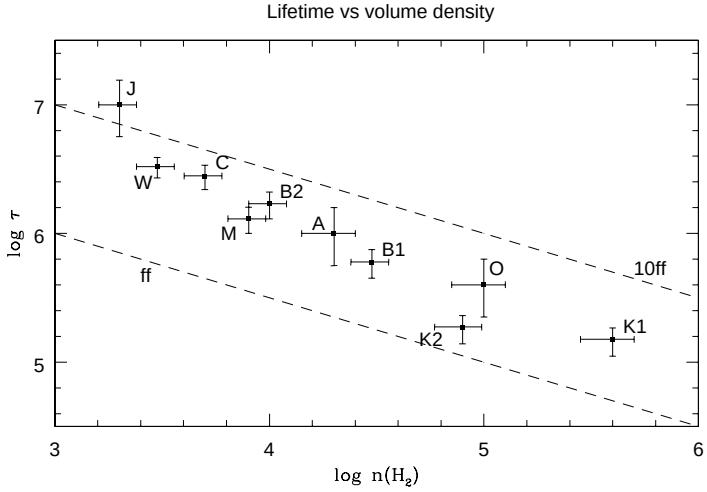

Fig. 11.6. Plot of inferred core lifetime against mean volume density for various samples of starless and prestellar cores. The two dashed lines correspond to one and ten free-fall times, respectively. (From Jessop & Ward-Thompson 2000 and Kirk et al. 2005.)

extinction at $A_V \sim 5 - 10$) for core formation (Onishi et al. 1998, Johnstone et al. 2004). Observationally, however, establishing the presence (or absence) of such a threshold is difficult since there are also detection thresholds. According to Hatchell et al. (2005), there is no real threshold but the probability of forming a prestellar core is a steeply rising function of background column density. In any case, the results of these wide-field surveys for cores clearly demonstrate the global inefficiency of the core formation process: the fraction of cloud mass observed in the form of prestellar cores is very low ($\lesssim 1 - 20\%$ – Hatchell et al. 2005, Nutter et al. 2006). Furthermore, there is some evidence that core/star formation in the observed cluster-forming clumps has been induced by external triggers (Nutter et al. 2006, Kirk et al. 2006). These results are broadly consistent with the view that the low-density envelopes of molecular clouds are supported against collapse by magnetic fields, as in the classical ambipolar diffusion picture (Mouschovias 1987, Shu et al. 1987, McKee 1989).

11.3.2.2 Core lifetimes

In the turbulent paradigm, cloud cores are always dynamically evolving (e.g. Dib et al. 2007) and survive for at most a few free-fall times.
Observationally, a rough estimate of the lifetime of starless cores can be ob-

tained from the number ratio of cores with and without embedded YSOs in a given core sample. Using this technique, Lee & Myers (1999) found that the typical lifetime of starless cores with average volume density $\sim 10^4$ cm^{-3} was $\sim 1 - 1.5 \times 10^6$ yr. Furthermore, by considering several samples of isolated cores spanning a range of core densities, Jessop & Ward-Thompson (2000) established that the typical core lifetime decreased as the mean volume density in the core sample increased (Fig. 11.6 – see also Kirk et al. 2005). As can be seen in Fig. 11.6, all of the observed lifetimes lie between one free-fall time, which is the timescale expected in free-fall collapse, and ten free-fall times, the timescale expected for highly subcritical cores undergoing ambipolar diffusion. The observed timescales are typically longer than the free-fall time by a factor of ∼2–5 in the density range of 10^4–10^5 cm^{-3}. This suggests that starless cores cannot all be rapidly evolving, at variance with purely hydrodynamic scenarios of core formation (e.g. Ballesteros-Paredes et al. 2003), but in agreement with numerical simulations of moderately supercritical, turbulent molecular clouds (Galván-Madrid et al. 2007). The observed timescales also appear to be too short for all of the cores to form from a highly subcritical state. These statistical estimates of core lifetimes are however quite uncertain since they assume that all of the observed cores follow the same evolutionary path and that the core/star formation rate is constant.

11.3.2.3 Magnetic field measurements

In principle, observations of magnetic fields can provide a strong discriminator between the two extreme paradigms of the core/star formation process. Two main observational techniques have been used to estimate the magnetic field strength in cloud cores. First, the Zeeman effect in, e.g., the 18-cm lines of OH, gives a direct measurement of the line-of-sight component of the magnetic field, but relatively few positive detections have been obtained. For existing detections, a very good correlation is found between the magnetic field strength B_{los} and $n^{0.5}\,\sigma_v$, where n is the gas density and σ_v is the line-of-sight velocity dispersion observed in optically thin molecular line tracers (Crutcher 1999, Basu 2000). This shows that magnetic fields play a dynamically important role during the contraction of at least some cloud cores and is consistent with cloud turbulence being MHD in character. Second, maps of linearly polarized dust emission at submillimeter wavelengths, combined with the Chandrasekhar and Fermi method, provide an indirect estimate of the plane-of-the-sky component of the magnetic field (e.g. Ward-Thompson et al. 2000, Crutcher et al. 2004). The available B-field measurements based on either the Zeeman technique or the Chan-

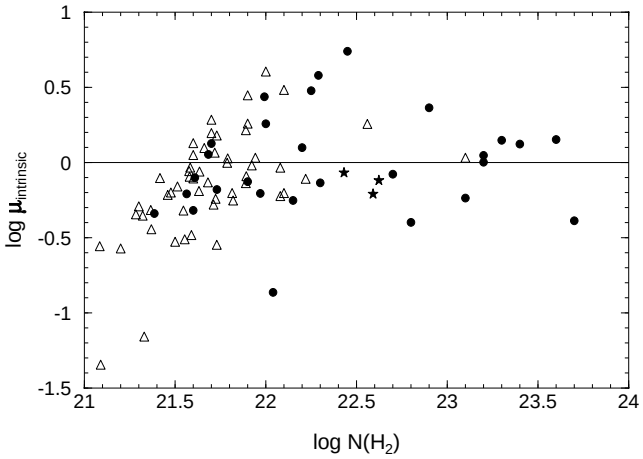

Fig. 11.7. Plot of observed mass-to-magnetic flux ratio, in units of the critical value and divided by 3 to correct for projection bias, against cloud/core column density. Dots are for Zeeman detections of $B_{\parallel}$ (above 3σ); stars are for Chandraskehar-Fermi estimates of $B_{\perp}$; open triangles are lower limits (corresponding to observed upper limits to the field strength). (From Heiles & Crutcher 2005 – see also Crutcher 2004 for details.)

drasekhar and Fermi method are summarized in Fig. 11.7 which plots the inferred mass-to-magnetic flux ratio corrected for projection effects against the column density of each core (see Crutcher 2004 and Heiles & Crutcher 2005). It can be seen that all cloud cores are scattered around the critical mass-to-flux ratio in this plot, suggesting that, on average, cores are close to magnetically critical. Furthermore, there is some hint in Fig. 11.7 that the mass-to-flux ratio may be systematically subcritical at column densities lower than $\sim 3 \times 10^{21}$ cm^{-3}. This tentative trend is weak, however, as it relies only on the locations of Zeeman non-detections in the diagram. Thus, existing magnetic field measurements do not allow a definite conclusion to be drawn, even if they seem to favor pictures of the core formation process in which the magnetic field does play an important role.

11.3.2.4 Radial density structure

The density profiles of isolated prestellar cores are now fairly well known. Two methods have been used: (1) mapping the optically thin (sub)millimeter continuum *emission* from the cold dust contained in the cores, and (2) mapping the same cold core dust in *absorption* against the background infrared emission (originating from warm cloud dust or remote stars).

Ward-Thompson et al. (1994, 1999) and André et al. (1996) employed

the first approach to probe the structure of prestellar cores (see also Shirley et al. 2000). Under the simplifying assumption of spatially uniform dust temperature and emissivity properties, they concluded that the radial density profiles of isolated prestellar cores were flatter than $\rho(r) \propto r^{-1}$ in their inner regions (for $r \leq R_{flat}$), and approached $\rho(r) \propto r^{-2}$ only beyond a typical radius $R_{flat} \sim$ 2500–5000 AU.

More recently, the use of the *absorption* approach, both in the mid-IR from space (e.g. Bacmann et al. 2000) and in the near-IR from the ground (e.g. Alves et al. 2001), made it possible to confirm and extend the (sub)millimeter emission results, essentially independently of any assumption about the dust temperature distribution. In some cases, such as L1689B, the absorption studies indicate that isolated prestellar cores feature sharp edges defining outer radii $R_{out} \sim 0.1$ pc (cf. Bacmann et al. 2000).

The circularly-averaged column density profiles can often be fit remarkably well with models of pressure-bounded Bonnor-Ebert spheres, as first demonstrated by Alves et al. (2001) for B68. This is also the case of cores detected in the submillimeter continuum such as L1689B (e.g. Kirk et al. 2005). The quality of the fits shows that equilibrium Bonnor-Ebert spheroids provide a good, first order model for the structure of isolated prestellar cores. In detail, however, there are problems with this model. First, the inferred density contrasts (from center to edge) are generally larger (i.e., $\gtrsim$ 20–80 – cf. Bacmann et al. 2000 and Kirk et al. 2005) than the maximum contrast of ~ 14 for stable Bonnor-Ebert spheres. Second, the effective gas temperature needed in the fits is often significantly larger than measured core temperatures (e.g. Ward-Thompson et al. 2002, Lai et al. 2003). These arguments suggest that prestellar cores are either already contracting (see Lee, Myers, Tafalla 2001 and § 11.3.2.5 below) or experiencing extra support from static or turbulent magnetic fields (e.g. Curry & McKee 2000). As shown by Bacmann et al. (2000), one way to account for large density contrasts and high effective temperatures is to consider models of cores initially supported by a static magnetic field and evolving through ambipolar diffusion (e.g. Ciolek & Mouschovias 1994, Basu & Mouschovias 1994).

However, good Bonnor-Ebert fits can often be found for dynamically evolving "cores" produced by turbulent compression (Ballesteros-Paredes et al. 2003, Gómez et al. 2007). Thus, the observed density profiles do not provide a very strong diagnostic of proposed core formation models.

11.3.2.5 Velocity structure

Observing the velocity field within and around dense cores is probably the most effective way to discriminate between quasi-static and dynamic core

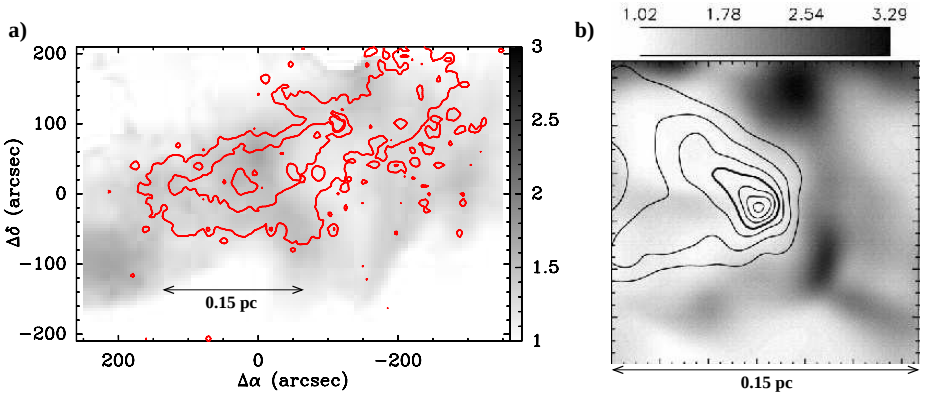

Fig. 11.8. a) Greyscale image of the line-of-sight velocity dispersion (in units of the isothermal sound speed) derived from deep ^{13}CO(1-0) line observations toward and around the prestellar core L1689B (from André, Pety, & Bacmann, in prep.). Column density contours from Bacmann et al. (2000) are superimposed and delineate the core boundaries. The maximum observed value of σ_{los} is only ~ 0.34 km/s or $\sim 1.7\,c_s$ b) Greyscale image of the line-of-sight velocity dispersion superimposed on column density contours for a model core obtained in SPH numerical simulations of gravoturbulent fragmentation (from Klessen et al. 2005). Note that these simulations produce localized maxima where $\sigma_{los} \gtrsim 3\,c_s$ at the shock positions.

formation scenarios. If cores are produced by shocks in large-scale supersonic flows, large-velocity gradients and local maxima of the line-of-sight velocity dispersion are expected in the immediate vicinity of cores (Ballesteros-Paredes et al. 2003; Klessen et al. 2005). A much more quiescent ambient velocity field is expected in the magnetically-controlled picture (e.g. Nakamura & Li 2005 – see also § 11.3.1 and Fig. 11.3).

Briefly, isolated starless cores are characterized by subsonic levels of internal turbulence (e.g. Myers 1983, Goodman et al. 1998, Caselli et al. 2002), small rotational velocity gradients (e.g. Goodman et al. 1993, Caselli et al. 2002), and extended, subsonic infall motions (e.g. Tafalla et al. 1998, Lee et al. 2001). Moreover, the environment of isolated prestellar cores is also extremely quiescent. This has been shown recently through deep mapping of several cores in low-density molecular gas tracers such as ^{13}CO(1–0) and C^{18}O(1–0). Figure 11.8a shows a greyscale map of the line-of-sight velocity dispersion σ_{los} observed in ^{13}CO(1–0) toward the prestellar core L1689B in the Ophiuchus complex (André et al. in prep.). It can be seen that σ_{los} remains at most transonic ($\sigma_{los} < 2\,c_s$, where c_s is the isothermal sound speed) everywhere in a region of more than 0.25 pc in diameter around the column density peak. Such a quiescent velocity field is at variance with

purely hydrodynamic models of gravoturbulent fragmentation (e.g. Klessen et al. 2005). While these models successfully produce a fair amount ($\sim 25\%$) of cores with subsonic internal velocity dispersions, corresponding to dense, post-shock stagnation points at the intersection of converging flows, they also produce highly supersonic maxima of σ_{los} in the low column density gas around the cores (cf. Fig. 11.8b), which are not observed. Current observations therefore provide strong indirect evidence that the evolution of isolated prestellar cores is magnetically controlled.

The environment of individual cores in cluster-forming regions is known to be more turbulent (e.g. Caselli & Myers 1995), so that hydrodynamic core formation models may be more appropriate in this case. Indeed, observations of Class 0 objects indicate that protostellar collapse is more dynamic, with supersonic infall velocities and large mass accretion rates ($> 10\, c_s^3/G$), in cluster-forming clumps (e.g. Di Francesco et al. 2001, Belloche et al. 2006). Evidence of coherent, supersonic contraction motions over more than 0.5 pc has even been found in some protoclusters (e.g. Motte et al. 2005, Peretto et al. 2006). On small scales, however, the compact (~ 0.03 pc) prestellar condensations of the Ophiuchus, Serpens, Perseus, and Orion protoclusters are themselves characterized by subsonic levels of internal turbulence (Myers 2001, André et al. 2007) reminiscent of the thermal cores of Taurus. Furthermore, the condensation-to-condensation velocity dispersion measured in these cluster-forming regions is small and only subvirial (André et al. 2007). This is consistent with the view that protoclusters often start their evolution from "cold", out-of-equilibrium initial conditions (cf. Adams et al. 2006), perhaps as a result of external perturbations (cf. Nutter et al. 2006). The observed small relative velocity dispersion also implies that collisions between condensations in a low-mass protocluster such as L1688 are relatively rare and that, in general, prestellar condensations do not have time to interact with one another before evolving into pre-main sequence objects (André et al. 2007). Furthermore, in such protoclusters, the mass accretion rate expected from competitive, Bondi-like accretion of background gas onto the condensations (e.g. Bonnell et al. 2001) is estimated to be at least a factor ~ 3 lower than the mass infall rate resulting from gravitational collapse at the Class 0 and Class I stages (André et al. 2007 – see also Krumholz et al. 2005). Therefore, competitive accretion cannot play a dominant role once individual protostellar collapse sets in. On the other hand, Bondi-like accretion of unbound gas is more effective before protostellar collapse, and may possibly govern the growth of starless, self-gravitating condensations initially produced by gravitational fragmen-

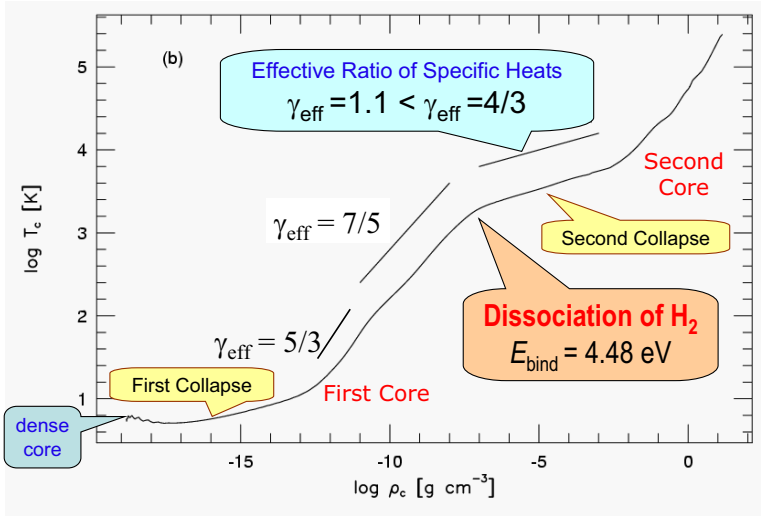

Fig. 11.9. Temperature evolution at the center of a gravitationally collapsing cloud obtained by Masunaga & Inutsuka (2000a) in their radiation hydrodynamical calculation of protostellar collapse in spherical symmetry. The *first collapse* phase corresponds to the formation of the *first protostellar core* that consists mainly of hydrogen molecules. The dissociation of hydrogen molecule triggers the *second collapse* that eventually produces the *second core*, i.e., a protostellar object. Each of these phases in the temperature evolution is characterized by a distinct value of the effective ratio of specific heats, $\gamma_{\rm eff}$.

tation (cf. § 11.3.1 and Fig. 11.4) toward a Salpeter-like IMF mass spectrum (cf. Myers 2000, Basu & Jones 2004, Clark & Bonnell 2005).

11.4 Collapse and subfragmentation of prestellar cores

11.4.1 Core collapse models: Thermodynamics

The evolution of gravitationally collapsing cores and the formation of protostars are radiation-magnetohydrodynamical processes. Although we need to model these processes by solving equations of radiative transfer and magnetohydrodynamics simultaneously in multi-dimensions, a direct calculation of all the equations remains challenging. The most sophisticated theoretical models so far are either non-magnetic radiation hydrodynamical calculations based on the (flux-limited) diffusion approximation or magnetohydrodynamical calculations with some prescribed equations of states.

Here, we first explain the thermodynamics of gravitational collapse revealed by dynamical modelling with detailed radiative transfer in *spherical* symmetry (Larson 1969; Narita, Nakano, & Hayashi 1970; Winkler & Newman 1980; Stahler, Shu, & Taam 1980; Masunaga, Miyama, & Inutsuka

1998; Masunaga & Inutsuka 2000a). The classical results based on gray-approximation were confirmed by recent work that solved the frequency-dependent RHD equations by the "Variable Eddington Factor Method" (Masunaga & Inutsuka 2000a). The latter provides the time evolution of the apparent spectrum of the radiation field (Spectral Energy Distribution – SED) in addition to the detailed dynamical evolution of the protostar.

Figure 11.9 shows the time evolution of the central temperature (as a function of the central density) in a collapsing cloud. Once compressional heating dominates over radiative cooling, the central temperature increases gradually above the low value ($\sim$ 10 K) found in molecular clouds. At first, the slope of the temperature curve corresponds to a ratio of specific heats $\gamma_{\rm eff} = 5/3$: $T(\rho) \propto \rho^{2/3}$ for $10\,{\rm K} < T < 10^2\,{\rm K}$. This apparently monoatomic gas behavior is due to the fact that the rotational degree of freedom of molecular hydrogen is not excited in this low temperature regime ($E(J = 2 - 0)/k_{\rm B} = 512$ K). When the temperature rises above $\sim 10^2$ K, the slope becomes that of diatomic molecules ($\gamma_{\rm eff} = 7/5$). In both cases, the effective ratio of specific heats is larger than the critical value for gas pressure support against self-gravity: $\gamma_{\rm eff} > \gamma_{\rm crit} \equiv 4/3$. Thus, the collapsing velocity is decelerated and forms a shock at the surface of quasi-adiabatic hydrostatic object, the "first core". Its radius is about 1 AU in spherically symmetric calculations (but is larger by an order of magnitude in 2D/3D calculations with rotation). It mainly consists of H_2. The increase in density and temperature inside the first core is slow but monotonic. When the temperature becomes $> 10^3$ K, the dissociation of H_2 starts. The binding energy of H_2 is about 4.5 eV which is much larger than the thermal energy per hydrogen molecule in this temperature regime. Therefore the dissociation of H_2 acts as an efficient coolant of the gas, which reduces the effective ratio of specific heats below the critical value ($\gamma_{\rm eff} < 4/3$), and triggers the second dynamical collapse†. In this "second collapse" phase, the collapsing velocity becomes very large and engulfs the first core. As a result, the first core lasts only for $\sim 10^3$ yr. In the course of the second collapse, the central density reaches a stellar value ($\rho_\star \sim 1\ {\rm g\,cm^{-3}}$), and a truly hydrostatic protostellar object forms in the center.

Radiation hydrodynamic (RHD) calculations automatically produce the time evolution of the accretion luminosity and SED of the collapsing object (cf. Masunaga & Inutsuka 2000a). The resultant luminosity evolution has a sharp growth at the formation of the first core and a peak around the formation of the second protostellar core in the case of dynamical initial

† Note that the role of H_2 dissociation in this second collapse is analogous to that of the photo-disintegration of Fe as the cause of the pre-supernova gravitational collapse.

conditions, while it only shows a gradual growth in the case of hydrostatic equilibrium initial conditions. This difference in the time evolution of the accretion luminosity may provide a useful observational diagnostic.

Molecular emission line profiles of various important species were also calculated in self-consistent dynamical models (Masunaga & Inutsuka 2000b). Recent three dimensional modelling of protostellar radiation hydrodynamics can be found, e.g., in Whitehouse & Bate (2006), Stamatellos et al. (2007b), and Krumholz et al. (2007).

Further evolution includes the T-Tauri phase on Hayashi tracks, for which the relevant (Kelvin-Helmholtz) timescale is about two orders of magnitude larger than the dynamical timescale ($\sim 10^5$ yr) of protostellar collapse, which is only accessible by steady state calculations (e.g. Chabrier & Baraffe 2000).

11.4.1.1 Dynamical roles of the first and second protostellar cores

The formation of the 'short-lived' first core plays an important role in the dynamical evolution of protostellar collapse, as well as the second core does. This is because the associated pressure support helps the formation of a rapidly rotating disk-like structure around the central object in the presence of non-zero initial angular momentum (Saigo, Matsumoto, & Hanawa 2000).

Rotationally-driven fragmentation into multiple systems: The mechanisms responsible for the formation of multiple systems have been the subject of extensive theoretical work (see, e.g., Goodwin et al. 2007 for a review). The essence of the results may be summarized as follows. First, gravitational sub-fragmentation within a collapsing cloud core is not expected during the early isothermal phase of evolution, unless the mass of the core is much larger than the initial Jeans mass. This result has been found in numerical simulations and is supported by semi-analytic calculations in the case of an initially uniform cloud with solid rotation (Tsuribe & Inutsuka 1999a,b). Initial central concentration in the density profile makes core fragmentation even more difficult. However, if the evolution is followed to the higher density regime where the gas becomes adiabatic, a disk-like structure forms which allows another mode of binary formation to develop, i.e., disk fragmentation around the central protostar. For example, calculations based on a piecewise polytropic equation of state show that the central portion of a collapsing core becomes adiabatic and forms a disc-like structure around the central object, which subsequently fragments into "satellite" objects (Matsumoto & Hanawa 2003). The study of realistic radiative transfer effects on these modes of binary fragmentation remains an important task for future work. The above phenomena correspond to the fragmentation

of/around the first core, which might account for the formation of binaries with separations $\gtrsim$ 1AU. Obviously formation of binaries with even shorter separations is also expected in the disk around the second protostellar core. These multiple epochs of core fragmentation may result in multiple peaks in the separation distribution of binary stars as proposed by Machida et al. (2007c).

The effects of initial turbulence on binary fragmentation have also been studied extensively (see, e.g., Goodwin et al. (2007). Purely hydrodynamic SPH simulations of rotating cloud core collapse show that a very low level of initial core turbulence (e.g. $E_{\rm turb}/E_{\rm grav} \sim 5\%$) leads to the formation of a multiple system (Goodwin et al. 2004; Hennebelle et al. 2004). In such hydrodynamic simulations, fragmentation is driven by a combination of rotation/turbulence and occurs in large ($\gtrsim$ 100 AU) disk-like structures or "circumstellar accretion regions" (CARs – cf. Goodwin et al. 2007). These CARs are highly susceptible to spiral instabilities which *always* fragment them into small-N *multiple systems with* $N > 2$ and typically $N \sim$ 3-4 within a radius $\sim$ 150 AU (Goodwin et al. 2004). However, recent MHD simulations of *magnetized* core collapse (Price & Bate 2007, Hennebelle & Teyssier 2008) show that the presence of an even moderate magnetic field strongly modifies angular momentum transport during collapse and at least partly suppresses core fragmentation. Therefore, it is unclear at the present time whether the collapse of an individual prestellar core typically produces one, two, or more stars.

Implications for the CMF-IMF connection: If each prestellar core is the progenitor of $N \sim 2-4$ stars, then the IMF of individual stars cannot be the direct product of the CMF but results instead from the convolution of the CMF with the typical distribution of object masses produced by binary fragmentation for one mass of core (cf. Delgado-Donate et al. 2003, Goodwin et al. 2008). For realistic binary fragmentation scenarios, the IMF will still follow the CMF at the high-mass end (because the majority of each core's mass can still end up in one stellar component), but may differ substantially from the CMF at the low-mass end. Such a picture is consistent with present determinations of the CMF (see § 11.2). However, it is presently unclear whether the collapse of an individual prestellar core typically produces one, two, or more stars. Accordingly, the origin of the low-mass end ($\lesssim 0.1\,M_{\odot}$) of the IMF is highly uncertain. Observationally, this is an area where the future large millimeter interferometer ALMA will yield key progress.

Driving MHD outflows: Another effect of the formation of the first core occurs in the MHD evolution of the self-gravitating collapsing core. A magnetically supercritical core whose rotation axis is parallel to the mean direction of the magnetic field lines leads to self-similar collapse as long as the equation of state is isothermal (Basu & Mouschovias 1994). Once the first core is formed, a rapidly rotating disk-like structure develops owing to the change in the effective equation of state, and its rapid rotation winds up the field lines creating a significant amount of toroidal magnetic field. This enhanced toroidal magnetic field produces a bipolar outflow driven by magnetic pressure (Tomisaka 2002). Thus, the formation of the first hydrostatic core plays a critical role in launching the protostellar outflow. A similar process happens again around the second core, with higher ejection velocities reminiscent of the observed optical jets and high-velocity neutral winds (Machida et al. 2006, 2007a, 2007b).

The observational detection of the first core would not only confirm the predictions of RHD modelling, but would also set strong constraints on MHD models of protostellar outflows as described in the next section.

11.4.2 Resistive MHD effects and onset of outflows

11.4.2.1 MHD modelling with resistivity

The full modelling of magnetohydrodynamical processes in star formation must include non-ideal MHD effects (e.g. Nakano et al. 2002, Tassis & Mouschovias 2007). Ambipolar diffusion is important at early times during the low-density core formation phase, but Ohmic dissipation is more important at later times in the high-density collapse phase. The Hall current term can also be important in an intermediate regime (Wardle 2004). To account for the dissipation of magnetic fields during the formation of protostars, Machida et al. (2006, 2007a, 2007b) used the resistive MHD equation with prescribed resistivity in their three-dimensional nested grid code simulations. Their basic equations are as follows:

$$\frac{\partial \rho}{\partial t} + \nabla \cdot (\rho \boldsymbol{v}) = 0, \tag{11.1}$$

$$\rho \frac{\partial \boldsymbol{v}}{\partial t} + \rho(\boldsymbol{v} \cdot \nabla)\boldsymbol{v} = -\nabla P - \frac{1}{4\pi}\boldsymbol{B} \times (\nabla \times \boldsymbol{B}) - \rho \nabla \phi, \tag{11.2}$$

$$\frac{\partial \boldsymbol{B}}{\partial t} = \nabla \times (\boldsymbol{v} \times \boldsymbol{B}) + \eta \nabla^2 \boldsymbol{B}, \tag{11.3}$$

$$\nabla^2 \phi = 4\pi G \rho, \tag{11.4}$$

where ρ, $\boldsymbol{v}$, P, $\boldsymbol{B}$, η, and ϕ denote the density, velocity, pressure, magnetic flux density, resistivity, and gravitational potential, respectively. Machida et al. estimated the resistivity η in equation (11.3) according to Nakano et al. (2002) and assumed that η was a function of density and temperature. They further assumed a barotropic equation of state to mimic the temperature evolution shown in Fig. 11.9. Hence η could be expressed as a function of density only: $\eta = c_\eta\, \eta_0(\rho)$, where $\eta_0(\rho)$ is a function of the central density. The initial conditions adopted by Machida et al. correspond to a spherical cloud with a critical Bonnor-Ebert density profile having a central (number) density $\rho_{c,0} = 3.841 \times 10^{-20}\,\mathrm{g\ cm^{-3}}$ ($n_{c,0} = 10^4\,\mathrm{cm^{-3}}$). In this case the critical Bonnor–Ebert sphere radius, $R_c = 6.45\, c_s [4\pi G \rho_{\mathrm{BE}}(0)]^{-1/2}$, corresponds to $R_c = 4.58 \times 10^4$ AU. The total mass inside the critical radius was $M_0 = 7.6\,\mathrm{M}_\odot$. Initially, the cloud was in solid body rotation around the z-axis (at a rate Ω_0) and had a uniform magnetic field ($B_{\mathrm{init}} = 17\mu\mathrm{G}$) parallel to the z-axis (or rotation axis). To promote contraction, the density was increased by 70% starting from the critical Bonnor-Ebert sphere.

The various models investigated by Machida et al. can be characterized by a single non-dimensional parameter ω, related to the cloud's initial rotation rate, and defined using the central density ρ_0 as $\omega = \Omega_0/(4\pi\, G\, \rho_0)^{1/2}$.The parameter ω, the initial magnetic field strength, the initial angular velocity Ω_0, the ratio of the thermal (α_0) and rotational (β_0) energies to the gravitational energy, the final magnetic field strength at the center, and the rotation period of the protostar at the final snapshot of the calculation are summarized in Table 11.2†, where SR, MR, and RR stand for (initially) slow, medium, and rapid rotator, respectively.

11.4.2.2 Protostellar outflows & jets

As a result of their calculations, Machida et al. found that two distinct flows (low- and high-velocity flows) are driven by the first and second cores.

† Representing the thermal, rotational, and gravitational energies as U, K, and W, the relative factors against the gravitational energy are defined as $\alpha_0 = U/|W|$, and $\beta_0 = K/|W|$.

Table 11.2. *Model Parameters and Results*

Model	ω	B_{init} [μG]	Ω_0 [s^{-1}]	α_0	β_0	B_{fin} (kG)	P_{fin} (day)
SR	0.003	17	7.0×10^{-16}	0.5	3×10^{-5}	2.18	3.0
MR	0.03	17	7.0×10^{-15}	0.5	3×10^{-3}	0.40	2.1
RR	0.3	17	7.0×10^{-14}	0.5	3×10^{-1}	—	—

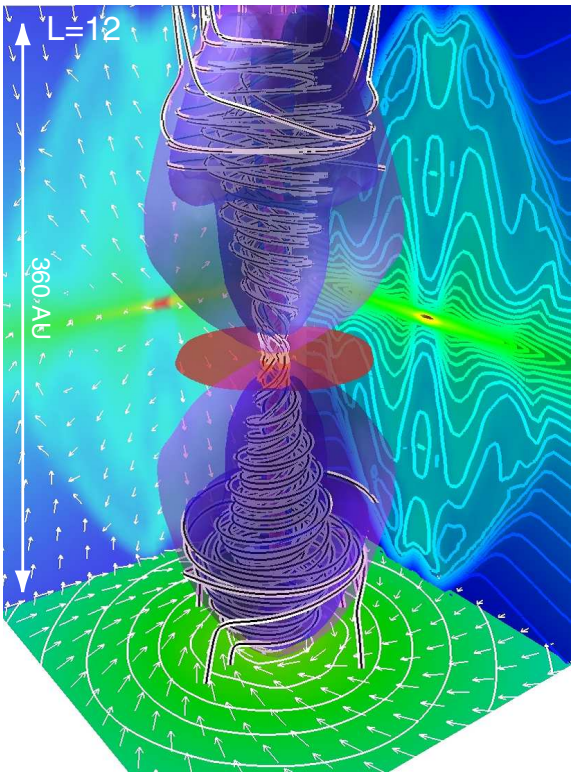

Fig. 11.10. Bird's-eye view of model RR ($l = 12$). The structure of high-density region ($n > 10^{12}\,\mathrm{cm}^{-3}$; iso-density surface), and magnetic field lines (black-and-white streamlines) are plotted. The structure of the outflow is shown by the iso-velocity surface inside which the gas is outflowing from the center. The density contours and velocity vectors (thin arrows) on the mid-plane of $x = 0$, $y = 0$, and $z = 0$ are, respectively, projected in each wall surface.

They proposed that the low-velocity flow from the first core corresponds to observed molecular outflows, while the high-velocity flow from the protostar corresponds to observed optical jets. As an illustration of their simulations, a snapshot of Model RR is shown in Fig. 11.10.

The results of Machida et al. show that the flow driven by the first core has a slow speed and a wide opening angle, while the flow driven by the protostar has a high speed and a well-collimated structure. The flow speed roughly corresponds to the escape speed of the driving object. The difference in the depth of the gravitational potential between the first and the second core therefore causes the difference in flow speed. Typically, observed molecular outflows and optical jets have speeds $v_{\mathrm{out,obs}} \simeq 30\,\mathrm{km\,s}^{-1}$ and $v_{\mathrm{jet,obs}} \simeq 100\,\mathrm{km\,s}^{-1}$, respectively. At the end of the calculations, the low-

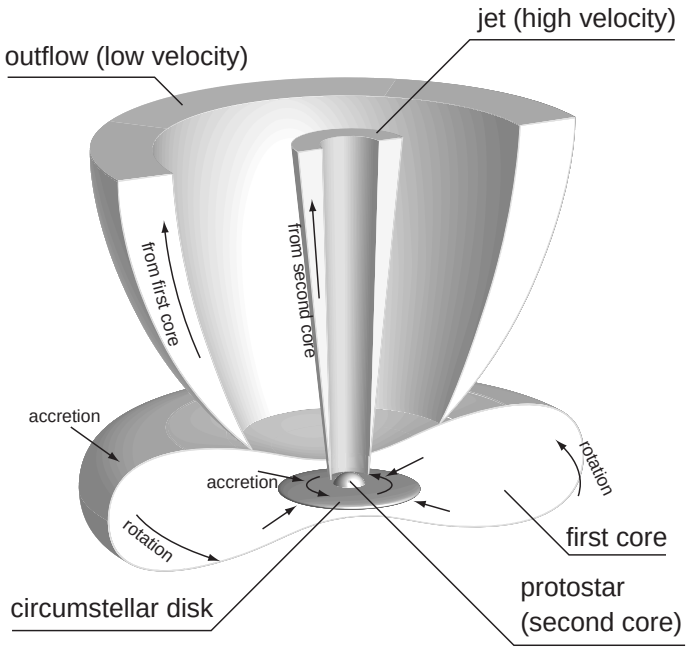

Fig. 11.11. Schematic picture proposed by Machida et al. (2007b) for the jet and outflow driven from the protostar and the fist core, respectively.

and high-velocity flows of Machida et al. only have speeds $v_{\rm LVF} \simeq 3\,{\rm km\,s^{-1}}$ and $v_{\rm HVF} \simeq 30\,{\rm km\,s^{-1}}$, respectively. However, the first and second cores only have masses $M_{\rm first\,core} = 0.01\,{\rm M_\odot}$ and $M_{\rm second\,core} \simeq 10^{-3}\,{\rm M_\odot}$, respectively, at the end of the calculations. Each core grows in mass by at least 1–2 orders of magnitude in the subsequent gas accretion phase. Since the escape speed increases as the square root of the mass of the central object at a fixed radius, the speeds of the low- and high-velocity flows may increase by a factor of ~ 10, and reach $v_{\rm LVF} \simeq 30\,{\rm km\,s^{-1}}$ and $v_{\rm HVF} = 300\,{\rm km\,s^{-1}}$, respectively, which correspond to typical observed values.

The difference in collimation between the two flows is caused both by different configurations of the magnetic field lines around the driving object and different driving mechanisms (see also Banerjee & Pudritz 2006 and Hennebelle & Fromang 2008). The magnetic field lines around the first core have an hourglass configuration because they converge to the cloud center as the cloud collapses, and Ohmic dissipation is ineffective before first core formation. Furthermore, the flow emerging near the first core is mainly a disk wind driven by the magnetocentrifugal wind mechanism. The centrifugal force is dominant in the low-velocity flow, whereas near the protostar,

the magnetic field lines are straight, and the magnetic pressure gradient mechanism is more effective in driving the high-velocity flow. The magnetic field lines are stretched by the magnetic tension force near the protostar because the magnetic field is decoupled from the neutral gas. However, the magnetic field lines are strongly twisted in the region in close proximity to the protostar, where the magnetic field is coupled with the neutral gas again. Thus, the strong toroidal field generated around the protostar can drive a high-velocity flow, which is guided by the straight configuration of the magnetic field.

Figure 11.11 summarizes the main features of the outflows and jets modelled by Machida et al. (2007b). Note that the calculations of Machida et al. cover only the very early phase of protostar evolution. Further longer-term calculations are needed to better understand the correspondence between the models and observed protostellar outflows.

11.4.2.3 Effects of outflows/jets on star-forming cores/clouds

In principle, outflows and jets from new-born stars may have strong dynamical effects on their environments. It has been proposed that the violent impact of fast outflows may result in the destruction of the cores from which the driving protostars are born (Nakano et al. 1995, Matzner & McKee 2000), or even in the dispersal of the parental molecular clouds. In particular, the local star formation efficiency at the level of individual cloud cores is most likely controlled by the effects of protostellar outflows: The model calculations of Matzner & McKee (2000) give $\epsilon_{\rm core} \equiv M_\star/M_{\rm core} \sim 25 - 75\%$ for various degrees of core flattening and magnetization. On a more global level, protostellar outflows may also significantly reduce the fraction of total molecular cloud mass going into stars. Thus, this process provides an interesting possibility for explaining the observed low star formation efficiency in the Galaxy.

Li & Nakamura (2006) proposed that protostellar outflows could also sustain a high level of turbulence in cluster-forming clouds, but Banerjee et al. (2007) argued that this was actually difficult. Obviously, a quantitative examination of all these processes will require appropriate dynamical modelling of protostellar outflows, which remains to be done both theoretically and observationally.

11.5 Conclusions: Proposed view for the star formation process

The prestellar core mass function (CMF) appears to be consistent with the stellar IMF between $\sim 0.1\,M_\odot$ and $\sim 5\,M_\odot$, although large uncertainties

remain especially at the low- and high-mass ends (cf. § 11.2). Small internal and relative motions are measured for these prestellar cores, implying that they are much less turbulent than their parent cloud and generally do not have time to interact before collapsing to (proto)stars (cf. § 11.3.2.5). These results strongly support scenarios according to which the IMF is largely determined at the prestellar stage.

None of the extreme scenarios proposed for the formation of prestellar cores can explain all observations. Pure ambipolar diffusion is too slow to be the main core formation mechanism, for typical levels of cloud ionization. Purely hydrodynamic pictures have trouble accounting for the inefficiency of core formation and the detailed velocity structure of individual cores. A mixed scenario (cf. Nakamura & Li 2005, Basu et al. 2008) may be the solution: supersonic MHD turbulence in a molecular cloud close to magnetic criticality generates seed cores, which grow in mass until they become gravitationally unstable and collapse in a magnetically-controlled fashion while decoupling from their turbulent environment. Such a mixed picture has several advantages. On the one hand, relatively strong magnetic fields prevent global collapse and lead to inefficient core/star formation on large (GMC) scales. On the other hand, the rate of ambipolar diffusion is enhanced by turbulence in shock-compressed regions (e.g. Zweibel 2002, Fatuzzo & Adams 2002, Nakamura & Li 2005). The difference between the clustered and the isolated or distributed mode of star formation may result from local variations around the critical mass-to-flux ratio and/or from the presence or absence of external triggers.

Cluster-forming clumps such as L1688 in Ophiuchus or NGC2264-C in Monoceros are likely (slightly) magnetically supercritical. There is some evidence that these clumps are in a state of global collapse induced by large-scale external triggers (e.g. Peretto et al. 2006, Nutter et al. 2006). In this case, the local star formation efficiency within each condensation is high ($\gtrsim 50\%$) and a promising core formation mechanism is purely gravitational, Jeans-like fragmentation of compressed cloud layers (cf. Palous 2007, Peretto et al. 2007), possibly followed by subsequent core growth (e.g. Basu & Jones 2004).

Regions of more distributed and less efficient star formation, such as Taurus or the Pipe Nebula, are likely slightly subcritical or nearly critical. The size of individual cores is then larger (e.g. Motte et al. 1998), the local star formation efficiency is lower ($\sim$ 15%–30% – Onishi et al. 2002, Alves et al. 2007), and the feedback from protostellar outflows may be more important in limiting accretion and defining stellar masses (e.g. Shu et al. 2004).

To fully understand how stars form and how the IMF comes about, a bet-

ter knowledge of the presently poorly known initial conditions for molecular cloud formation is required, a subject of growing interest (see, e.g., Hennebelle et al. in this volume). It is also crucial to further investigate the processes by which prestellar cores form, evolve, and eventually collapse and fragment into multiple protostellar systems. With present submillimeter instrumentation, observational studies are limited by small-number statistics and restricted to the nearest regions. The advent of major new facilities in the coming years should yield several breakthroughs in this field. With an angular resolution at 75–300 μm comparable to, or better than, the largest ground-based millimeter-wave radiotelescopes, *Herschel*, the Far InfraRed and Submillimeter Telescope to be launched by ESA in 2008 (cf. Pilbratt 2005), will make possible complete surveys for prestellar cores down to the proto-brown dwarf regime in the cloud complexes of the Gould Belt (cf. André & Saraceno 2005). High-resolution ($0.01'' - 0.1''$) studies with the 'Atacama Large Millimeter Array' (ALMA, becoming partly available in 2011, fully operational in 2013 – cf. Bachiller 2008) at ~ 450 μm – 3 mm will allow us to probe the kinematics of individual condensations in distant, massive protoclusters. Complementing each other nicely, *Herschel* and ALMA will tremendously improve our global understanding of the initial stages of star formation in the Galaxy.

References

Adams, F. C., Proszkow, E. M., Fatuzzo, M., & Myers, P. C. 2006, ApJ, 641, 504

Alves, J. F., Lada, C. J., & Lada, E. A. 2001, Nature, 409, 159

Alves, J. F., Lombardi, M., & Lada, C. J. 2007, A&A, 462, L17

André, P., Belloche, A., Motte, F., & Peretto, N. 2007, A&A, 472, 519

André, P. & Montmerle, T. 1994, ApJ, 420, 837

André, P. , & Saraceno, P. 2005, in The Dusty and Molecular Universe: A Prelude to *Herschel* and ALMA, ESA SP-577, p. 179

André, P., Ward-Thompson, D., & Barsony, M. 1993, ApJ, 406, 122

André, P., Ward-Thompson, D., & Barsony, M. 2000, in Protostars and Planets IV, ed. V. Mannings, A. Boss, & S. Russell (Tucson: Univ. Arizona Press), 59

André, P., Ward-Thompson, D., & Motte, F. 1996, A&A, 314, 625

Bachiller, R. (Ed.) 2008, Science with ALMA: A new era for Astrophysics, (Springer: Berlin), Ap&SS, in press

Bacmann, A., André, P., Puget, J.-L., Abergel, A., Bontemps, S., & Ward-Thompson, D. 2000, A&A, 361, 555

Ballesteros-Paredes, J., Klessen, R. S., & Vázquez-Semadeni, E. 2003, ApJ, 592, 188

Ballesteros-Paredes, J., Gazol, A., Kim, J., Klessen, R. S. et al. 2006, ApJ, 637, 384

Banerjee, R., & Pudritz, R. E. 2006, ApJ, 641, 949

Banerjee, R., Klessen, R. S., & Fendt, C. 2007, ApJ, 668, 1028

Basu, S. 2000, ApJ, 540, L103
Basu, S., & Ciolek, G. E. 2004, ApJ, 607, L39
Basu, S., & Jones, C. E. 2004, MNRAS, 347, L47
Basu S., & Mouschovias T. Ch. 1994, ApJ, 432, 720
Basu, S., Ciolek, G. E., & Wurster, J. 2008, New Astronomy, submitted
Basu, S., Ciolek, G. E., Dapp, W., & Wurster, J. 2008, in preparation
Bate, M. R., & Bonnell, I. A. 2005, MNRAS, 356, 1201
Bate, M. R., Bonnell, I. A., & Bromm, V. 2003, MNRAS, 339, 577
Belloche, A., Hennebelle, P., & André, P. 2006, A&A, 453, 145
Benson, P. J., Myers, P. C. 1989, ApJS, 71, 89
Blitz, L. 1993, in Protostars & Planets III, Eds. E. H. Levy and J. I. Lunine (Tucson: Univ. of Arizona Press), p. 125
Bonnell, I. A., Bate, M. R., Clarke, C. J., & Pringle, J. E. 2001, MNRAS, 323, 785
Caselli, P., & Myers, P. C. 1995, ApJ, 446, 665
Caselli, P., Benson, P. J., Myers, P. C., & Tafalla, M. 2002, ApJ, 572, 238
Chabrier, G. & Baraffe, I. 2000, ARA&A 38, 337
Chabrier, G. 2005, in The Initial Mass Function 50 years later, Eds. E. Corbelli et al., p.41
Ciolek, G. E., & Basu, S. 2006, ApJ, 652, 442
Ciolek, G. E., & Mouschovias, T. Ch. 1994, ApJ, 425, 142
Clark, P. C. & Bonnell, I. A. 2005, MNRAS, 361, 2
Clark, P. C., Klessen, R. S., & Bonnell, I. A. 2007, MNRAS, 379, 57
Crutcher, R. M. 1999, ApJ, 520, 706
Crutcher, R. M. 2004, Ap&SS, 292, 225
Crutcher, R. M., Nutter, D. J., Ward-Thompson, D., & Kirk, J. 2004, ApJ, 600, 279
Curry, C. L., & McKee, C. F. 2000, ApJ, 528, 734
Delgado-Donate, E. J., Clarke, C. J., & Bate, M. R. 2003, MNRAS, 342, 926
Dib, S., Kim, J., Vázquez-Semadeni, E., Burkert, A., & Shadmehri, M. 2007, ApJ, 661, 262
Di Francesco, J., Myers, P. C., Wilner, D. J., Ohashi, N., & Mardones, D. 2001, ApJ, 562, 770
Elmegreen, B. G. 1979, ApJ, 232, 729
Elmegreen, B. G. 1997, ApJ, 486, 944
Elmegreen, B. G. 2000, in Star Formation from the Small to the Large Scale, Eds. F. Favata, A. A. Kaas & A. Wilson, ESA SP-445, 265
Elmegreen, B. G., & Falgarone, E. 1996, ApJ, 471, 816
Fatuzzo, M. & Adams, F. C. 2002, ApJ, 570, 210
Enoch, M. L., Young, K. E., Glenn, J., Evans, N. J. et al. 2006, ApJ, 638, 293
Galván-Madrid, R., Vázquez-Semadeni, E., Kim, J., & Ballesteros-Paredes, J. 2007, ApJ, 670, 480
Gómez, G. C., Vázquez-Semadeni, E., Shadmehri, M., & Ballesteros-Paredes, J. 2007, ApJ, 669, 1042
Goodman, A. A., Benson, P. J., Fuller, G. A., & Myers, P. C. 1993, ApJ, 406, 528
Goodman, A. A., Barranco, J. A., Wilner, D. J., & Heyer, M. H. 1998, ApJ, 504, 223
Goodwin, S., Whitworth, A., & Ward-Thompson, D. 2004, A&A, 414, 633
Goodwin, S. P., Kroupa, P., Goodman, A., & Burkert, A. 2007, in Protostars and Planets V, ed. B. Reipurth et al. (Tucson: Univ. Arizona Press), 133

Goodwin, S. P., Nutter, D., Kroupa, P., Ward-Thompson, D., & Whitworth, A. 2008, A&A, 477, 823
Gregersen, E. M., & Evans, N. J. II 2000, ApJ, 538, 260
Hartmann, L. 2002, ApJ, 578, 914
Hatchell, J., Richer, J. S., Fuller, G. A., Qualtrough, C. J., Ladd, E. F., & Chandler, C. J. 2005, A&A, 440, 151
Heiles, C., & Crutcher, R. M. 2005, in Cosmic Magnetic Fields, Eds. R. Wielebinski & R. Beck, LNP, 664, 137
Hennebelle, P. & Fromang, S. 2008, A&A, 477, 9
Hennebelle, P. & Teyssier, R. 2008, A&A, 477, 25
Hennebelle, P., Whitworth, A., Cha, S.-H, & Goodwin, S. 2004, MNRAS, 348, 687
Inutsuka, S. 2001, ApJ, 559, L149
Inutsuka, S. & Miyama, S. M. 1992, ApJ, 388, 392
Inutsuka, S. & Miyama, S. M. 1997, ApJ, 480, 681
Jessop, N. E., & Ward-Thompson, D. 2000, MNRAS, 311, 63
Jijina, J., Myers, P. C., & Adams, F. C. 1999, ApJS, 125, 161
Johnstone, D., Wilson, C. D., Moriarty-Schieven, G., Joncas, G., Smith, G., Gregersen, E., & Fich, M. 2000, ApJ, 545, 327
Johnstone, D., Fich, M., Mitchell, G. F., Moriarty-Schieven, G. 2001, ApJ, 559, 307
Johnstone, D., Di Francesco, J., & Kirk, H. 2004, ApJ, 611, L45
Johnstone, D., Matthews, H., & Mitchell, G. F. 2006, ApJ, 639, 259
Kirk, J. M., Ward-Thompson, D., & André, P. 2005, MNRAS, 360, 1506
Kirk, H., Johnstone, D., & Di Francesco, J. 2006, ApJ, 646, 1009
Klessen, R. S., & Burkert, A. 2000, ApJS, 128, 287
Klessen, R. S., Ballesteros-Paredes, J., Vázquez-Semadeni, E., & Durán-Rojas, C. 2005, ApJ, 620, 786
Kramer, C., Stutzki, J., Rohrig, R., Corneliussen, U. 1998, A&A, 329, 249
Kroupa, P. 2001, MNRAS, 322, 231
Krumholz, M. R., McKee, C. F., & Klein, R. I. 2005, Nature, 438, 332
Krumholz, M. R., Klein, R. I., & McKee, C. F. 2007, ApJ, 656, 959
Kudoh, T., Basu. S., Ogata, Y., & Yabe, T. 2007, MNRAS, 380, 499
Kudoh, T., & Basu. S. 2008, ApJL, submitted
Lada, C. J. 1987, in Star Forming Regions, Eds. M. Peimbert & J. Jugaku (Reidel, Dordrecht), IAU Symp. 115, 1
Lada, C. J., Muench, A. A., Rathborne, J. M., Alves, J., & Lombardi, M. 2008, ApJ, in press
Lai, S.-P., Velusamy, T., Langer, W. D., & Kuiper, T. B. H. et al. 2003, AJ, 126, 311
Larson, R. B. 1969, MNRAS, 145, 271
Larson, R. B. 1981, MNRAS, 194, 809
Larson, R. B. 1985, MNRAS, 214, 379
Larson, R. B. 2005, MNRAS, 359, 211
Lee, C. W., & Myers, P. C. 1999, ApJS, 123, 233
Lee, C. W., Myers, P. C., & Tafalla, M. 2001, ApJS, 136, 703
Li, Z.-Y., & Nakamura, F. 2004, ApJ, 609, L83
Li, Z.-Y. & Nakamura, F. 2006, ApJ 640, L187
Lombardi, M., & Bertin, G. 2001, A&A, 375, 1091
McKee, C. F. 1989, ApJ, 345, 782
Mac Low, M.-M., & Klessen, R. S. 2004, RvMP, 76, 125

Machida, M. N., Inutsuka, S., & Matsumoto, T. 2006, ApJ, 647, L151
Machida, M. N., Inutsuka, S., & Matsumoto, T. 2007a, ApJ, 670, 1198
Machida, M. N., Inutsuka, S., & Matsumoto, T. 2007b, ApJ, in press (arXiv:0705.2073)
Machida, M. N., Tomisaka, K, Matsumoto, T., & Inutsuka, S. 2007c, ApJ, submitted (arXiv:0709.2739)
Masunaga, H., Miyama, S. M. & Inutsuka, S. 1998, ApJ, 495, 346
Masunaga, H. & Inutsuka, S. 1999, ApJ, 510, 822
Masunaga, H. & Inutsuka, S. 2000, ApJ, 531, 350
Masunaga, H. & Inutsuka, S. 2000, ApJ, 536, 406
Matsumoto, T. & Hanawa, T. 2003, ApJ, 595, 913
Matsumoto T., & Tomisaka K. 2004, ApJ, 616, 266
Matzner, C. & McKee, C. 2000, ApJ, 545, 364
Motte, F., André, P., & Neri, R. 1998, A&A, 365, 440
Motte, F., André, P., Ward-Thompson, D., & Bontemps, S. 2001, A&A, 372, L41
Motte, F., Bontemps, S., Schilke, P., Lis, D., Schneider, N., & Menten, K. 2005, in "Massive star birth: a crossroads of astrophysics", IAU Symp. 227, Eds. R.Cesaroni et al., Cambridge University Press, p. 151
Motte, F., Bontemps, S., Schilke, P., Schneider, N., Menten, K. M., & Broguière, D. 2007, A&A, 476, 1243
Mouschovias, T. Ch. 1987, in Physical Processes in Interstellar Clouds, ed. G. E. Morfill & M. Scholer (Dordrecht: Reidel), 453
Myers, P. C. 1983, ApJ, 270, 105
Myers, P. C. 2000, ApJ, 530, L119
Myers, P. C. 2001, in From Darkness to Light, Eds. T. Montmerle & P. André, ASP Conf. Ser., 243, 131
Nagai, T., Inutsuka, S.-I., & Miyama, S. M. 1998, ApJ, 506, 306
Nakamura, F., & Li, Z.-Y. 2005, ApJ, 631, 411
Nakano, T. 1979, PASJ, 31, 697
Nakano, T., Hasegawa, T., & Norman, C. 1995, ApJ, 450, 183
Nakano, T., Nishi, R., & Umebayashi, T. 2002, ApJ, 573, 199
Narita, S., Nakano, T., & Hayashi, C. 1970, Prog. Theor. Phys., 43, 942
Nutter, D., Ward-Thompson, D., & André, P. 2006, MNRAS, 368, 1833
Nutter, D., & Ward-Thompson, D. 2007, MNRAS, 374, 1413
Onishi, T., Mizuno, A., Kawamura, A., Ogawa, H., Fukui, Y. 1998, ApJ, 502, 296
Onishi, T., Mizuno, A., Kawamura, A., Tachihara, K., & Fukui, Y. 2002, ApJ, 575, 950
Padoan, P. & Nordlund, A. 2002, ApJ, 576, 870
Palous, J. 2007, in Triggered Star Formation in a Turbulent ISM, IAU Symp. 237, Eds. B. G. Elmegreen & J. Palous, Cambridge University Press, p. 114
Peretto, N., André, P., & Belloche, A. 2006, A&A, 445, 979
Peretto, N., Hennebelle, P., & André, P. 2007, A&A, 464, 983
Pilbratt, G. 2005, in The Dusty and Molecular Universe: A Prelude to *Herschel* and ALMA, ESA SP-577, p. 3
Price, D. J., & Bate, M. R. 2007, MNRAS, 377, 77
Reid, M. A. & Wilson, C. D. 2006, ApJ, 650, 970
Saigo, K., Matsumoto, T., & Hanawa, T. 2000, ApJ, 531, 971
Salpeter, E. E. 1955, ApJ, 121, 161
Shirley, Y., Evans II, N. J., Rawlings, J. M. C., Gregersen, E. M. 2000, ApJS, 131, 249

Shu, F. H., Adams, F. C., & Lizano, S. 1987, ARA&A, 25, 23
Shu, F. H., Li, Z.-Y., Allen, A. 2004, ApJ, 601, 930
Simon, R. 1965, Annales d'Astrophysique, 28, 40
Spitzer, L., Jr. 1942, ApJ, 95, 329
Stahler, S. W., Shu, F. H., & Taam, R. E. 1980, ApJ, 241, 637
Stamatellos, D., Whitworth, A. P., & Ward-Thompson, D. 2007a, MNRAS, 379, 1390
Stamatellos, D., Whitworth, A. P., Bisbas, T., & Goodwin, S. 2007b A&A 475, 37
Stanke, T., Smith, M. D., Gredel, R., & Khanzadyan, T. 2006, A&A, 447, 609
Tafalla, M., Mardones, D., Myers, P. C., Caselli, P., Bachiller, R., & Benson, P. J. 1998, ApJ, 504, 900
Tassis, K. & Mouschovias, T. Ch. 2007, ApJ, 660, 370
Testi, L., & Sargent, A. I. 1998, ApJ, 508, L91
Tilley, D. A., & Pudritz, R. E. 2007, MNRAS, 382, 73
Tomisaka, K. 2002, ApJ, 575, 306
Tsuribe, T., & Inutsuka, S. 1999, ApJ, 523, L155
Tsuribe, T., & Inutsuka, S. 1999, ApJ, 526, 307
Vázquez-Semadeni, E., Kim, J., Shadmehri, M., & Ballesteros-Paredes, J. 2005, ApJ, 618, 344
Wardle, M. 2004, Ap&SS, 292,317
Ward-Thompson, D., André, P., & Kirk, J. M. 2002, MNRAS, 329, 257
Ward-Thompson, D., André, P., Crutcher, R., Johnstone, D., Onishi, T., & Wilson, C. 2007, Protostars and Planets V, Eds. B. Reipurth, D. Jewitt, K. Keil (Tucson: University of Arizona Press), p. 33
Ward-Thompson, D., Kirk, J. M., Crutcher, R. M., Greaves, J. S., Holland, W. S., & André, P. 2000, ApJ, 537, L135
Ward-Thompson, D., Motte, F., & André, P. 1999, MNRAS, 305, 143
Ward-Thompson, D., Scott, P. F., & Hills, R. E., & André, P. 1994, MNRAS, 268, 276
Whitehouse, S. C., & Bate, M. R. 2006, MNRAS, 367, 32
Winkler, K.-H. A., & Newman, M. J. 1980, ApJ, 236, 201; 1980, ApJ, 238, 311
Zuckerman, B., & Palmer, P. 1974, ARA&A, 12, 279
Zweibel, E. G. 2002, ApJ, 567, 962